

# Diffusion of muonic hydrogen in hydrogen gas and the measurement of the 1s hyperfine splitting of muonic hydrogen

J. Nuber<sup>1,2\*</sup>, A. Adamczak<sup>3</sup>, M. Abdou Ahmed<sup>4</sup>, L. Affolter<sup>2</sup>, F. D. Amaro<sup>5</sup>, P. Amaro<sup>6</sup>, P. Carvalho<sup>6</sup>, Y.-H. Chang<sup>7</sup>, T.-L. Chen<sup>7</sup>, W.-L. Chen<sup>7</sup>, L. M. P. Fernandes<sup>5</sup>, M. Ferro<sup>6</sup>, D. Goeldi<sup>2</sup>, T. Graf<sup>4</sup>, M. Guerra<sup>6</sup>, T. W. Hänsch<sup>8,9</sup>, C. A. O. Henriques<sup>5</sup>, M. Hildebrandt<sup>1</sup>, P. Indelicato<sup>10</sup>, O. Kara<sup>2</sup>, K. Kirch<sup>1,2</sup>, A. Knecht<sup>1</sup>, F. Kottmann<sup>1,2</sup>, Y.-W. Liu<sup>7</sup>, J. Machado<sup>6</sup>, M. Marszalek<sup>1,2</sup>, R. D. P. Mano<sup>5</sup>, C. M. B. Monteiro<sup>5</sup>, F. Nez<sup>10</sup>, A. Ouf<sup>11</sup>, N. Paul<sup>10</sup>, R. Pohl<sup>11,12</sup>, E. Rapisarda<sup>1</sup>, J. M. F. dos Santos<sup>5</sup>, J. P. Santos<sup>6</sup>, P. A. O. C. Silva<sup>5</sup>, L. Sinkunaite<sup>1,2</sup>, J.-T. Shy<sup>7</sup>, K. Schuhmann<sup>2</sup>, S. Rajamohanam<sup>11</sup>, A. Soter<sup>2</sup>, L. Sustelo<sup>6</sup>, D. Taqqu<sup>1,2</sup>, L.-B. Wang<sup>7</sup>, F. Wauters<sup>12,13</sup>, P. Yzombard<sup>10</sup>, M. Zeyen<sup>2</sup>, J. Zhang<sup>2</sup>, A. Antognini<sup>1,2†</sup>

<sup>1</sup> Paul Scherrer Institute, 5232 Villigen-PSI, Switzerland

<sup>2</sup> Institute for Particle Physics and Astrophysics, ETH Zurich, 8093 Zurich, Switzerland

<sup>3</sup> Institute of Nuclear Physics, Polish Academy of Sciences, PL-31342 Krakow, Poland

<sup>4</sup> Institut für Strahlwerkzeuge, Universität Stuttgart, 70569 Stuttgart, Germany

<sup>5</sup> LIBPhys-UC, Department of Physics, University of Coimbra, P-3004-516 Coimbra, Portugal

<sup>6</sup> Laboratory of Instrumentation, Biomedical Engineering and Radiation Physics (LIBPhys-UNL), Department of Physics, NOVA School of Science and Technology, NOVA University Lisbon, 2829-516 Caparica, Portugal

<sup>7</sup> LPhysics Department, National Tsing Hua University, Hsincho 300, Taiwan

<sup>8</sup> Ludwig-Maximilians-Universität, Fakultät für Physik, 80799 Munich, Germany

<sup>9</sup> Max Planck Institute of Quantum Optics, 85748 Garching, Germany

<sup>10</sup> Laboratoire Kastler Brossel, Sorbonne Université, CNRS, ENS-Université PSL, Collège de France, 75005 Paris, France

<sup>11</sup> QUANTUM, Institute of Physics, Johannes Gutenberg-Universität Mainz, 55099 Mainz, Germany

<sup>12</sup> Excellence Cluster PRISMA+, Johannes Gutenberg-Universität Mainz, 55099 Mainz, Germany

<sup>13</sup> Institute of Nuclear Physics, Johannes Gutenberg-Universität Mainz, 55099 Mainz, Germany

\*jonas.nuber@psi.ch †aldo.antognini@psi.ch

December 26, 2022

## Abstract

The CREMA collaboration is pursuing a measurement of the ground-state hyperfine splitting (HFS) in muonic hydrogen ( $\mu\text{p}$ ) with 1 ppm accuracy by means of pulsed laser spectroscopy. In the proposed experiment, the  $\mu\text{p}$  atom is excited by a laser pulse from the singlet to the triplet hyperfine sub-levels, and is quenched back to the singlet state by an inelastic collision with a  $\text{H}_2$  molecule. The resulting increase of kinetic energy after this cycle modifies the  $\mu\text{p}$  atom diffusion in the hydrogen gas and the arrival time of the  $\mu\text{p}$  atoms at the target walls. This laser-induced modification of the arrival times is used to expose the atomic transition. In this paper we present the simulation of the  $\mu\text{p}$  diffusion in the  $\text{H}_2$  gas which is at the core of the experimental scheme. These simulations have been implemented with the Geant4 framework by introducing various low-energy processes including the motion of the  $\text{H}_2$  molecules, i.e. the effects related with the hydrogen target temperature. The simulations

have been used to optimize the hydrogen target parameters (pressure, temperatures and thickness) and to estimate signal and background rates. These rates allow to estimate the maximum time needed to find the resonance and the statistical accuracy of the spectroscopy experiment.

---

## Contents

<b>1</b>	<b>Introduction</b>	<b>2</b>
<b>2</b>	<b>The experimental scheme</b>	<b>3</b>
<b>3</b>	<b><math>\mu\text{p-H}_2</math> collisional processes</b>	<b>4</b>
<b>4</b>	<b>Monte Carlo simulations of molecular collisions</b>	<b>6</b>
4.1	Scattering rates in the laboratory reference system	6
4.2	Implementation in Geant4 of the molecular collisions at low energy	8
<b>5</b>	<b>Kinetic energy of the <math>\mu\text{p}</math> atoms after the cascade process</b>	<b>8</b>
<b>6</b>	<b>Simulations of the <math>\mu\text{p}</math> diffusion in the HFS experiment</b>	<b>9</b>
6.1	Thermalization and $\mu\text{p}$ diffusion prior to the arrival of the laser pulse	9
6.2	Laser excitation	12
6.3	Diffusion after the laser excitation	14
<b>7</b>	<b>Signal and background rates and target optimization</b>	<b>17</b>
<b>8</b>	<b>Search and scan of the HFS resonance</b>	<b>20</b>
<b>9</b>	<b>Conclusion</b>	<b>23</b>
	<b>References</b>	<b>24</b>

---

## 1 Introduction

Highly accurate measurements of atomic transitions in muonic atoms can be used as precise probes of low-energy properties of nuclei. While the measurement of the  $2s - 2p$  transitions in light muonic atoms were used for the determination of nuclear charge radii and polarizability contributions [1–4], the measurement of the ground state hyperfine splitting (HFS) in muonic hydrogen ( $\mu\text{p}$ ), an atom formed by a negative muon and a proton, can be used to advance the current understanding of the magnetic structure of the proton [5–15].

Three collaborations are aiming for the measurement of the HFS in muonic hydrogen with precision on the ppm level by means of pulsed laser spectroscopy [16–18]. Comparing the measured HFS with the corresponding theoretical prediction [5, 7, 19, 20] will result in a precise

determination of the two-photon exchange contribution which is to be compared with predictions from chiral perturbation theory [7, 10, 21], and data-driven approaches based on dispersion relations [9, 11, 12, 22].

The aim of this study (which is part of a PhD thesis [23]) is to describe and simulate the diffusion of  $\mu p$  atoms in hydrogen ( $H_2$ ) gas which is at the core of the HFS experiment of the CREMA collaboration. The corresponding measurement will take place at a muon beamline of the CHRISP facility [24] at the Paul Scherrer Institute (PSI) in Switzerland. This study allows us to estimate background and signal rates, to optimize the experimental design and to define the minimal requirements for the laser system, optical cavity and target. Moreover, it enables an estimation of the maximum time needed to find the resonance and the statistical accuracy which can be reached in the HFS measurement.

In Sec. 2 we introduce the principle and the experimental setup of the CREMA HFS measurement, highlighting the role of the diffusion processes, which we aim to quantify in this study. In Sec. 3 we introduce the collisional processes between the  $\mu p$  atom and the  $H_2$  molecules and their related cross sections and collision rates. How these collisional processes are implemented using Geant4 taking into account also the thermal motion of the  $H_2$  molecules is presented in Sec. 4. An important input for the diffusion simulations is the kinetic energy distribution of the  $\mu p$  atoms after their formation. This is discussed in Sec. 5. In Sec. 6 we present the results obtained from the diffusion simulations while in Sec. 7 we apply these simulations to determine signal and background rates and to optimize the target parameters. Estimates of the maximum time needed to search for the resonance and of the accuracy of the spectroscopy measurement can be obtained from the simulated signal and background rates, which is discussed in Sec. 8.

## 2 The experimental scheme

The principle of the HFS experiment by the CREMA Collaboration is illustrated in Fig. 1. A negative muon of about 11 MeV/c momentum passes an entrance detector triggering the laser system and is stopped in a cryogenic  $H_2$  gas target wherein  $\mu p$  in a highly excited state is formed. While the laser pulse is being generated, the  $\mu p$  atom quickly deexcites to the  $1s$  state. Through collisions with the  $H_2$  molecules, the  $\mu p$  atom ends up at the  $F = 0$  (singlet) sublevel of the ground state while thermalizing to the  $H_2$  gas temperature of 22 K. After  $\sim 1 \mu s$ , the  $\mu p$  atom is thermalized and the generated laser pulse of about 1 mJ energy at a wavelength of 6.8  $\mu m$  (corresponding to 0.18 eV) is coupled into a multi-pass toroidal cavity surrounding the muon stopping region. The multiple reflections of the laser pulse occurring in this cavity allow the illumination of a disk-shaped volume in the center of the target with a diameter of 15 mm and a thickness of 0.5 mm (see Fig. 1). The on-resonance laser pulse may then excite the  $\mu p$  atom from the singlet ( $F = 0$ ) to the triplet ( $F = 1$ ) sublevels. A successful excitation of the  $\mu p$  atoms to the triplet state is followed within 10 ns by an inelastic collision between the  $\mu p$  atom and a  $H_2$  molecule that deexcites the  $\mu p$  atom back to the singlet sublevel. In this process, the HFS transition energy is converted into kinetic energy so that the  $\mu p$  atom acquires on average 0.1 eV of kinetic energy. Because this energy is much higher than the thermal energy, the  $\mu p$  atom can quickly diffuse out of the laser-illuminated volume and reach one of the target walls coated with gold. When the  $\mu p$  reaches the gold-coated walls, the negative muon of the  $\mu p$  atom is transferred to a gold atom forming muonic gold ( $\mu Au^*$ ) in a highly excited state. Through a cascade of mainly radiative deexcitation, the  $\mu Au^*$  quickly reaches the ground state after the emission of several x rays of MeV energy

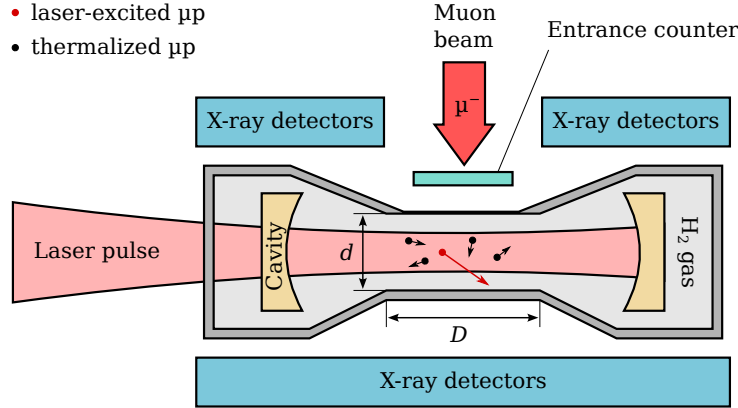
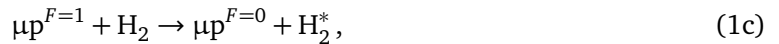


Figure 1: Schematic (not to scale) of the setup for measuring the HFS transition. The  $\mu p$  atoms are formed in a hydrogen gas target (22 K, 0.6 bar) within a volume of thickness  $d \approx 1$  mm (target thickness) and diameter  $D \approx 15$  mm. If excited by the laser, the  $\mu p$  atoms gain 0.1 eV kinetic energy and can diffuse efficiently towards the target walls. At the wall, the muons are transferred to gold atoms and form muonic gold atoms in highly excited states. The X-rays produced during the subsequent deexcitation of the muonic gold atoms are detected outside of the target cell.

which can be detected as a signature of a successful laser excitation. The HFS resonance can thus be obtained by counting the number of  $\mu\text{Au}^*$  cascade processes (referred in the following as  $\mu\text{Au}$  events) in a certain time window (event time window) after the laser excitation as a function of the laser frequency.

### 3 $\mu p\text{-H}_2$ collisional processes

In this section we provide an introduction to the  $\mu p\text{-H}_2$  scattering processes relevant for this study. There are four molecular scattering processes relevant for  $\mu p$  atoms in the  $1s$  state which are classified according to the initial and final hyperfine states (total spin  $F$ ), that can assume the values  $F = 0$  or  $F = 1$ :



The superscript “\*” indicates that the rotational-vibrational state of  $\text{H}_2$  can be altered by the scattering process. Hence, none of these processes are strictly-speaking elastic but we refer to the processes of Eqs. (1a) and (1d) as “elastic” in the sense that the total spin state  $F$  of the  $\mu p$  atom is conserved.

In the collisions described by Eqs. (1), the hyperfine state of the  $\mu p$  atoms can be either conserved or changed by a spin-flip reaction, in which the muon is transferred to a proton of the  $\text{H}_2$  molecule. These transfer reactions can thus lead to transitions between the two hyperfine levels depending on the spin of the proton to which the muon has been transferred. Note that the de-

excitation rate of the upper spin state ( $F = 1$ ) at the typical target conditions is several orders of magnitude larger than the muon decay rate, which is in turn several orders of magnitude larger than the radiative deexcitation rate [17, 25].

Calculations of the differential cross sections for the processes in Eqs. (1)(a-d) use the cross sections for the corresponding "nuclear" scattering processes of  $\mu p$  on single protons, for which scattering amplitudes are available [26–28]. In addition, they take into account effects of molecular binding of the protons in  $H_2$ , electron screening and spin correlations for specific rotational states of  $H_2$ . A method for calculating the partial differential cross sections of these processes is described in Refs. [29, 30] and the numerical results for the cross sections are tabulated for energies  $\leq 100$  eV in Ref. [29]. The total cross sections  $\sigma_{if}^{CM}$  are given in Fig. 2 as a function of collision

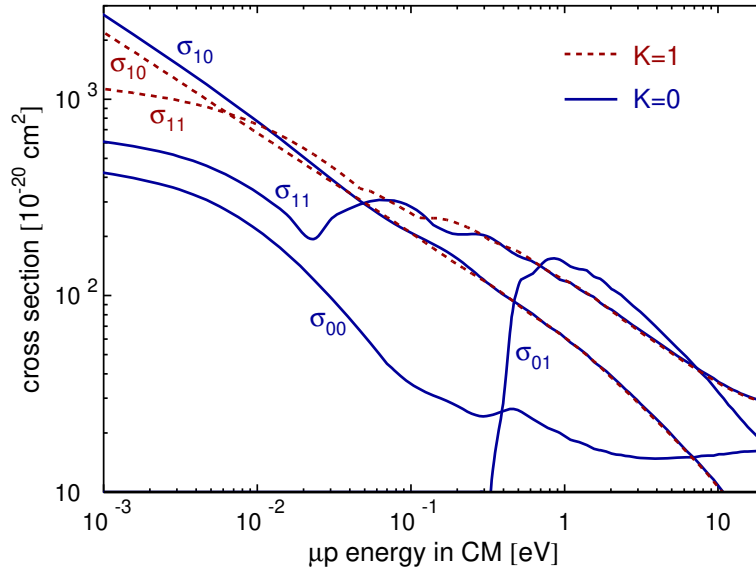


Figure 2: Total cross sections for the processes given in Eqs. (1) as a function of the CM energy, for two initial rotational states of the hydrogen molecule:  $K = 0$  and  $K = 1$ . The first and second indices denote the initial and the final hyperfine states, respectively. Since the cross sections  $\sigma_{00}$  and  $\sigma_{01}$  for both initial rotational states practically do not differ, these cross sections are plotted for  $K = 0$  only.

energy in the center of mass (CM) frame of the  $\mu p + H_2$  system. The indices  $i, f \in \{0, 1\}$  denote the total spin of the initial and final hyperfine states, respectively. These cross sections account for all possible ro-vibrational excitations of the  $H_2$  molecule.

The blue curves have been calculated assuming that all the  $H_2$  molecules are in the rotational state  $K = 0$  prior to a collision. For comparison, the cross sections  $\sigma_{10}^{CM}$  and  $\sigma_{11}^{CM}$  are also given assuming all  $H_2$  molecules are in the  $K = 1$  rotational state prior to collision. As can be seen from the figure, minor differences between the two cross sections can only be found below 0.05 eV, which are due to the spin correlations and different values of rotational thresholds for the two initial rotational levels. It is also interesting to note that the cross section  $\sigma_{01}$  has a threshold at a CM energy of  $\sim 0.3$  eV corresponding to the minimum energy needed for upscattering the  $\mu p$  atom from the lower lying singlet state to the triplet state.

## 4 Monte Carlo simulations of molecular collisions

To simulate the diffusion process of  $\mu\text{p}$  atoms in the  $\text{H}_2$  gas, we have implemented the molecular scattering processes of Eqs. (1) as custom physics processes in the Monte Carlo toolkit Geant4 [31], which we used via the program G4beamline [32]. In this section, we discuss how these physics processes were implemented using energy-dependent double-differential cross sections of the molecular collisions and taking into account the thermal motion of the  $\text{H}_2$  molecules.

### 4.1 Scattering rates in the laboratory reference system

To use the scattering cross sections discussed in Sec. 3, the cross sections need to be transformed from the center-of-mass to the laboratory (LAB) reference system. In this transformation, the thermal motion of the  $\text{H}_2$  molecule can not be neglected as the  $\mu\text{p}$  energy is similar to the thermal energy of the  $\text{H}_2$  molecules. As the Geant4 program does not account for the motion (prior to collision) of target particles, we define effective collision rates (from which the mean free path length needed by Geant4 can be deduced) that account for the thermal motion of the  $\text{H}_2$  molecules.

In the CM system, the total collision rates  $\Gamma_{\text{if}}^{\text{CM}}$  are defined as:

$$\Gamma_{\text{if}}^{\text{CM}} = \rho v_{\text{rel}} \sigma_{\text{if}}^{\text{CM}}, \quad (2)$$

where  $\rho$  is the number density of  $\text{H}_2$  molecules and  $v_{\text{rel}}$  denotes the relative velocity of  $\mu\text{p}$  and  $\text{H}_2$ . The partial differential rates  $\partial^2 \Gamma_{\text{if}} / (\partial E' \partial \Omega)$  in the LAB system can be obtained from the calculated differential cross sections  $\partial^2 \sigma_{\text{if}}^{\text{CM}} / (\partial E'_{\text{CM}} \partial \Omega_{\text{CM}})$  in the CM system:

$$\frac{\partial^2 \Gamma_{\text{if}}(E(v))}{\partial E' \partial \Omega} = \frac{\rho}{2} \sum_{E'_{\text{CM}}, \Omega_{\text{CM}}} \int dV g_M(V) \int_{-1}^1 dz_\alpha v_{\text{rel}}(V, z_\alpha; v) \frac{\partial^2 \sigma_{\text{if}}^{\text{CM}}(E_{\text{CM}})}{\partial E'_{\text{CM}} \partial \Omega_{\text{CM}}}, \quad (3)$$

where  $E$ ,  $E'$ ,  $\Omega$  and  $E_{\text{CM}}$ ,  $E'_{\text{CM}}$ ,  $\Omega_{\text{CM}}$  denote the initial and final  $\mu\text{p}$  energies and the solid scattering angle in LAB and CM system, respectively. The relative velocity,  $v_{\text{rel}}$ , depends on the  $\mu\text{p}$  speed ( $v$ ), on the  $\text{H}_2$  speed ( $V$ ) – both of them in the LAB reference system – and on  $z_\alpha = \cos(\alpha)$ , where  $\alpha$  is the impact angle. The  $\text{H}_2$  velocities are described by the Maxwell-Boltzmann distribution  $g_M$  at a temperature  $T$ . The summation over  $E'_{\text{CM}}$  and  $\Omega_{\text{CM}}$  includes only contributions to the small intervals  $\delta E'$  around  $E'$  and  $\delta \Omega$  around  $\Omega$  from the differential cross section in CM system. Finally, the rate is averaged over a distribution of the initial rotational energy levels for a given  $\text{H}_2$  target, which is denoted by the horizontal line.

The calculated total rates  $\Gamma_{\text{if}}$  of the processes given in Eqs. (1) are shown in Fig. (3) as functions of the  $\mu\text{p}$  kinetic energy for a target temperature of 22 K and for a liquid hydrogen density (LHD)  $\rho_0 = 2.125 \times 10^{22}$  molecules/cm<sup>3</sup>. The results are shown for two distributions of the initial rotational states of  $\text{H}_2$  molecules. The Boltzmann distribution corresponds to the distribution of rotational states in hydrogen gas in thermal equilibrium. At 22 K this means that practically all  $\text{H}_2$  molecules are in the state  $K = 0$ . The 3:1 distribution instead denotes a mixture of the states  $K = 1$  and  $K = 0$  that corresponds to the degeneracy of both levels (3:1), as it is present in  $\text{H}_2$  gas at room temperature. When cooling down hydrogen gas to 22 K, the gas will remain with the 3:1 rotational distribution for a long time (weeks at the conditions of the HFS experiment) because the relaxation process from  $K = 1$  to  $K = 0$  is very slow [33].

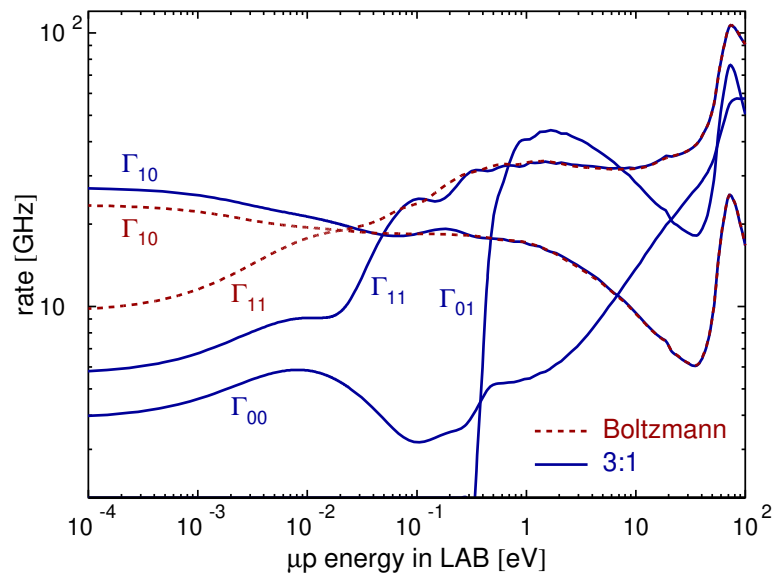


Figure 3: Collision rates  $\Gamma_{if}$  for the processes given in Eqs. (1) calculated from Eq. (3) as a function of the  $\mu p$  collision energy in the LAB reference frame at 22 K and liquid hydrogen density. The indices  $i$  and  $f$  denote the total spin of the initial and final hyperfine states, respectively. We considered both the Boltzmann and the 3:1 distribution of the initial rotational states of the  $H_2$  molecules. Analogously to the cross sections  $\sigma_{00}$  and  $\sigma_{01}$  shown in Figure 2, the rates  $\Gamma_{00}$  and  $\Gamma_{01}$  are not sensitive to the initial rotational distribution, and are therefore plotted for the Boltzmann distribution only.

## 4.2 Implementation in Geant4 of the molecular collisions at low energy

For efficient implementation of the the LAB rates of Eq. (3) into Geant4, we export them in data tables. For each initial  $\mu\text{p}$  energy,  $E$ , a table storing the double-differential cross section for various final energies,  $E'$ , and scattering angles,  $\theta$ , is generated. In each  $\mu\text{p}$ - $\text{H}_2$  scattering process,  $E'$  and  $\theta$  are sampled randomly from these two-dimensional distributions at the given energy  $E$ , while the azimuthal angle can simply be sampled from a uniform distribution.

All four molecular scattering processes of Eqs. (1) were implemented as discrete processes in Geant4 using the following procedure. Each process proposes a step length by randomly sampling from a Poissonian distribution with an expectation value given by the mean free path length. The scattering process and the actual step length (distance travelled between two subsequent collisions) are then given by the smallest of the proposed step lengths.

To calculate the mean free paths  $\lambda_{\text{if}}$  for these processes at a given initial energy,  $E$ , we first calculate the total rates  $\Gamma_{\text{if}}(E)$  by integrating the right side of Eq. (3) and then use

$$\lambda_{\text{if}}(E) = \frac{v(E)}{\Gamma_{\text{if}}(E)}, \quad (4)$$

where  $v(E)$  is the speed of the  $\mu\text{p}$  atom in the LAB system having an energy  $E$ .

## 5 Kinetic energy of the $\mu\text{p}$ atoms after the cascade process

For the simulations of  $\mu\text{p}$  diffusion in the  $\text{H}_2$  gas, knowledge of the  $\mu\text{p}$  kinetic energy right after the formation and deexcitation to the ground state is needed. However, the atomic formation process and the subsequent deexcitation mechanisms are highly complex, which makes it difficult to assess the energy of  $\mu\text{p}$  after reaching the  $1s$  state.

The  $\mu\text{p}$  atoms are created in collisions of slow ( $\sim 10$  eV) negative muons with  $\text{H}_2$  molecules leading to the formation of  $\mu\text{p}$  atoms in highly excited states with principal quantum number  $n \approx 14$  [34]. The formation of the excited  $\mu\text{p}$  atoms is followed by a fast ( $\sim 10^{-10}$  s for a density of  $\varphi = 10^{-2}$ , given in fractions of the liquid hydrogen density  $\rho_0$ ) deexcitation process (cascade) to the  $1s$  state, which involves radiative transitions, external Auger effects, Stark mixing, Coulomb transitions, elastic and inelastic scattering, and dissociation of  $\text{H}_2$  molecules. The cascade model on which this work is based, which shows a good agreement with experimental data, is summarized in Ref. [35].

Apart from the radiative deexcitations, all processes occur in collisions with surrounding  $\text{H}_2$  molecules. Thus, the rates of these processes depend on the target density, as well as on the collision energy. For these reasons the most recent cascade model [36, 37] also traces the kinetic energy evolution in addition to the evolution of the atomic state. Indeed, the various cascade processes may lead to acceleration or deceleration of the excited  $\mu\text{p}$  atoms.

The main acceleration of the  $\mu\text{p}$  atoms occurs through Coulomb deexcitations in which the transition energy from  $n$  to  $n'$  is converted into kinetic energy shared between the colliding partners (the  $\mu\text{p}$  atom and an  $\text{H}_2$  molecule). In the Coulomb  $7 \rightarrow 6$ ,  $6 \rightarrow 5$ ,  $5 \rightarrow 4$ ,  $4 \rightarrow 3$ , and  $3 \rightarrow 2$  transitions with  $\Delta n = 1$ , the  $\mu\text{p}$  atoms acquire 9, 15, 27, 58 and 166 eV kinetic energy, respectively. Coulomb deexcitations with  $\Delta n > 1$  lead to larger kinetic energies but are suppressed compared to  $\Delta n = 1$ . The acceleration from Auger processes is smaller as the electron carries away the largest fraction of the transition energy, while the radiative transitions do not significantly affect the kinetic energy of the  $\mu\text{p}$  atoms as the recoil energies are only of the order of few meV. On the



other hand, Stark transitions, elastic and inelastic collisions with or without excitation of the  $\text{H}_2$  molecules are the processes which decelerate the  $\mu\text{p}$  atoms down to thermal energies.

For our diffusion simulations we chose an initial (right after the deexcitation to the  $1s$ -state)  $\mu\text{p}$  energy distribution that roughly approximates the distribution given in Fig. 4 of Ref. [35]. For simplicity, we assume that 50 % of the  $\mu\text{p}$  atoms have a kinetic energy of 1 eV, and the other 50 % are uniformly distributed between 0 and 100 eV. In the following, this initial energy distribution will be referred to as the 50/50 distribution. Even though this seems a crude approximation, it is sufficient for our purposes as the results do not depend on the details of the distribution. The upper limit of 100 eV was imposed by the fact that no cross sections are available above this energy. As we shall see later, the optimal target density for the HFS experiment is  $0.008 \leq \varphi \leq 0.01$  (given in fractions of the liquid hydrogen density), which is approximately a factor of 2 smaller than the density used to simulate the kinetic energy distribution reported in Fig. 4 of Ref. [35]. Hence, for the HFS experiment, we expect in general a shift of the initial kinetic energies to lower values compared to Fig. 4 of Ref. [35]. The kinetic energy assumed in this study is thus a conservative estimate yielding conservative predictions of the signal rate. To investigate the sensitivity of the results to the choice of the initial energy distribution and to give a lower limit of the signal rate we also simulate the diffusion process assuming that all the  $\mu\text{p}$  atoms have an initial kinetic energy of 100 eV.

## 6 Simulations of the $\mu\text{p}$ diffusion in the HFS experiment

This section presents the simulation of  $\mu\text{p}$  atom diffusion in the  $\text{H}_2$  gas accounting for the low-energy processes described above. For clarity, this section is divided in three parts. The first describes  $\mu\text{p}$  thermalization and diffusion before laser excitation (see Sec. 6.1). The second section provides some information on the laser excitation probability and depicts the kinetic energy distribution of the  $\mu\text{p}$  atoms after a successful cycle of laser excitation and subsequent collisional deexcitation (see Sec. 6.2). The third section provides details on the diffusion of  $\mu\text{p}$  atoms after laser excitation until they reach one of the target walls (see Sec. 6.3).

### 6.1 Thermalization and $\mu\text{p}$ diffusion prior to the arrival of the laser pulse

A muon passing the entrance detector triggers the laser system and then enters through a thin foil into the  $\text{H}_2$  gas target with a thickness of about 1 mm in beam direction. Depending on the gas density, only about 10-20 % (see later for more details) of the muons are eventually stopped in the  $\text{H}_2$  gas forming  $\mu\text{p}$ . In this subsection we describe the thermalization of the  $\mu\text{p}$  atoms after they have deexcited to the ground state, how they are quenched to the singlet sublevel, and how many of them remain in the hydrogen gas while the laser system is building up the pulse.

Because the target is very thin compared to the width of the stopping range, in these simulations we generate the  $\mu\text{p}$  atoms homogeneously distributed over the target thickness. We assume a stopping volume with a diameter  $D = 15$  mm (see Fig. 1) corresponding approximately to the muon beam size. We note that the results, for symmetry reasons, are insensitive to the exact transverse distribution. We also assume an initial kinetic energy distribution corresponding to the 50/50 distribution described in Sec. 5, and an initial population of the  $\mu\text{p}$  hyperfine sublevels following the statistical distributions: 75 % in the triplet state and 25 % in the singlet state.

Figure 4a shows the evolution of the mean kinetic energy of the  $\mu\text{p}$  atoms after the atomic cascade following the  $\mu\text{p}$  formation, simulated for various temperatures and densities  $\varphi$ . For

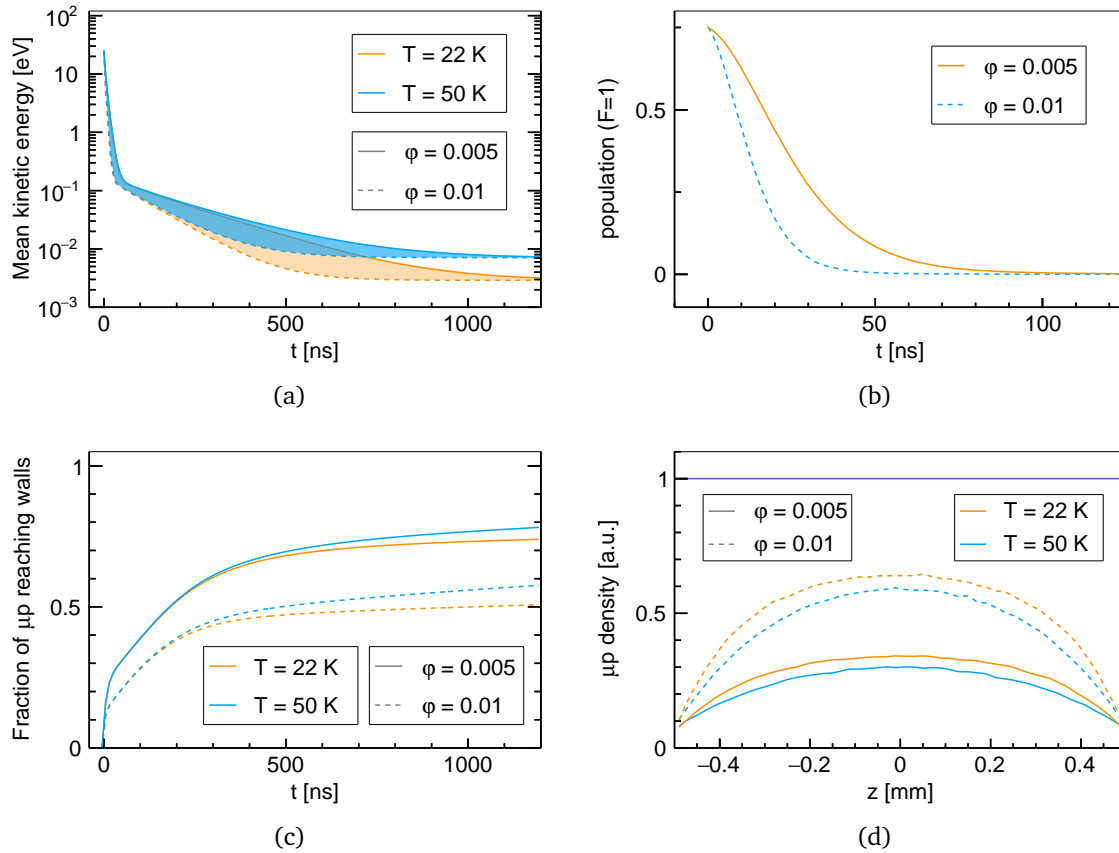


Figure 4: (a) Time evolution of the average (LAB frame) kinetic energy of the  $\mu p$  atom. (b) Time evolution of the population in the triplet state. (c) Fraction of  $\mu p$  atoms that has reached either of the target walls. (d) Spatial distribution of the  $\mu p$  atoms 1  $\mu s$  after their formation for a target of thickness  $d = 1$  mm. The horizontal line represents the distribution at time  $t = 0$  when the muonic atoms are formed. In all these plots we assumed that 50% of the  $\mu p$  atoms have an initial kinetic energy of 1 eV and for the other 50% the initial energy is distributed uniformly between 0 and 100 eV. Initially, 75% of the  $\mu p$  atoms are assumed to be in the triplet state.

example, a density of  $\varphi = 0.01$  corresponds to a pressure of about 0.6 bar at 22 K or 1.4 bar at 50 K. Throughout the paper we define as  $t = 0$  the time of the muonic atom formation. The cascade time is negligibly short on the  $\mu\text{s}$  time scale of the experimental sequence.

As can be seen from the time evolution, within 1  $\mu\text{s}$  – which corresponds to the time needed for the laser system to deliver the pulse – the  $\mu\text{p}$  are thermalized at the  $\text{H}_2$  gas temperature. We anticipate here that the optimal target condition for a target of 1.0 mm thickness and 22 K is  $\varphi = 0.01$ , while for a target of 1.2 mm thickness it is  $\varphi = 0.008$ .

The time evolution of the kinetic energy exhibits two slopes which are a consequence of the energy threshold of the up-scattering reaction from  $F = 0$  to  $F = 1$  described by  $\Gamma_{01}$  (see Fig. 3). With mean energies far above the up-scattering threshold, both hyperfine sublevels are populated and there are continuous transitions between these two sublevels given by the rates  $\Gamma_{01}$  and  $\Gamma_{10}$ . Hence, all four processes given in Eqs. (1) are occurring, leading to a fast energy loss and a large slope in the kinetic energy plot. When the energy drops below the up-scattering threshold of  $\sim 0.3$  eV, the up-scattering rate  $\Gamma_{01}$  vanishes and all  $\mu\text{p}$  atoms quickly deexcite to the  $F = 0$  state. A simulation of the  $F = 1$  population shown in Fig. 4b confirms this behavior. Since the deexcitation happens at energies much higher than thermal energies, the given behaviour is not dependent on the temperature. The only collisional process that is still occurring below this threshold is thus the elastic scattering for the singlet sublevel with rate  $\Gamma_{00}$ , which is the smallest compared to the other rates as visible from Fig. 3. For these reasons, for energies below the up-scattering energy threshold, the thermalization proceeds at a much slower pace.

At the target conditions of the HFS experiment, the  $\mu\text{p}$  atoms with kinetic energies of a few tens of eV have mean free paths of a few hundred  $\mu\text{m}$ . Hence, a significant fraction of the  $\mu\text{p}$  atoms formed in the hydrogen gas can diffuse into the target walls where the muon is transferred to the gold atoms and is lost for the spectroscopy experiment. Figure 4c shows the fraction of  $\mu\text{p}$  atoms arriving at either of the target walls versus time assuming a target thickness of 1 mm and that the initial energies of the  $\mu\text{p}$  atoms follow the 50/50 distribution discussed in Sec. 5. As visible from the figure, between 50 and 80% of the total formed  $\mu\text{p}$  atoms are lost prior to the laser excitation, depending on the target conditions. Note that temperature effects only emerge when the kinetic energy of the  $\mu\text{p}$  approaches thermal energies. On top of this, the losses due to muon decay (not included in these simulations) have to be considered: when the laser pulse arrives in the target at  $t = 1$   $\mu\text{s}$ , the number of surviving  $\mu\text{p}$  atoms has been further reduced by a factor of  $\exp(-1/2.2) = 0.63$  (muon lifetime  $\tau_\mu = 2.2$   $\mu\text{s}$ ).

It is interesting to also consider how the spatial distribution of the  $\mu\text{p}$  atoms evolves with time. Figure 4d shows the distribution of the  $\mu\text{p}$  atoms along the 1 mm thick target at 1  $\mu\text{s}$  after the muonic atom formation for various density and temperature conditions. The various curves are normalized to the number of  $\mu\text{p}$  atoms at time  $t = 0$  (see blue horizontal line) when the muonic atoms are formed. Due to the low density of the hydrogen gas, the muon stopping distribution in the gas and the  $\mu\text{p}$  distribution at  $t = 0$  were assumed to be flat. Also in this plot, the decay losses (which do not modify the shape of the distribution) are not included and we assume the 50/50 distribution for the initial energy of the  $\mu\text{p}$  atoms. The shape of the distribution changes with time (especially in first few hundreds of nanoseconds when the  $\mu\text{p}$  kinetic energies are large) because the walls of the target act as sinks for the  $\mu\text{p}$  atoms, so that the initial homogeneous distribution eventually develops a broad maximum centered in the target mid-plane.

## 6.2 Laser excitation

After deexciting to the singlet state  $F = 0$  and reaching thermal equilibrium with the hydrogen gas, the  $\mu\text{p}$  atoms are ready to be excited to the triplet state  $F = 1$  by the laser pulse. In Ref. [17] we calculated the combined probability that a  $\mu\text{p}$  atom – initially in the singlet state and thermalized at  $\text{H}_2$  temperature – undergoes a laser transition to the triplet state followed by a collisional-induced deexcitation back to the singlet state. This probability accounts for de-coherence effects caused by collisions and laser bandwidth as well as the Doppler broadening.

To enhance the transition probability and to efficiently illuminate the muon stopping volume, the laser pulses are coupled into a multi-pass cavity. We designed a toroidal multi-pass cavity, as shown in Fig. 5a, that allows the illumination of a disk-shaped volume, in which the light is coupled through a tiny slit and undergoes multiple reflections at the mirror surface. The illuminated volume is matched to the geometry of the hydrogen gas target which has been chosen to be thin (in the  $z$ -direction) to allow the laser excited  $\mu\text{p}$  atoms to reach one of the target walls with high probability. In contrast, the region of interest in the transverse direction is given by the size of the muon beam with a diameter of about 15 mm. More details about the multi-pass cavity will be published elsewhere; here we give only the main features relevant for this study. Detailed studies of the fluence distribution and the performance of the cavity are included in Ref. [38]. Information about the laser system can be found, e.g., in Ref. [39].

The fluence distribution of the toroidal cavity has been simulated with a ray tracing program. In the  $z$ -direction, the cavity is stable and the input beam is mode-matched so that the light-distribution in this direction is Gaussian with a  $1/e^2$  radius (waist) of only 0.18 mm close to the center of the cavity (see Fig. 5b). In the transverse plane the cavity is unstable so that the pulses bouncing back and forth in the cavity spread out with time, resulting in a radial distribution as shown in Fig. 5c. The fluence distribution has been computed assuming an in-coupled pulse of 1 mJ energy, a mirror reflectivity of 0.992 (as measured for a copper cavity) and a cavity diameter of 100 mm. At these conditions, the lifetime of the light in the cavity is 40 ns to be compared with the laser pulse length expected to be around 30-50 ns. The plots of Figs. 5b and 5c also depict the fluence-dependent excitation probability, showing small saturation effects even for relatively large fluences.

At the hydrogen gas conditions of the HFS measurement, the laser-excited  $\mu\text{p}$  atoms undergo an inelastic collision with a hydrogen molecule within 10 ns. In this collisional induced deexcitation, the  $\mu\text{p}$  atoms get a share of the 0.18 eV transition energy, acquiring on average about 0.1 eV. The exact kinetic energy distribution after the collisionally-induced deexcitation computed using the double-differential cross sections is shown in Fig. 6. For comparison, the kinetic energy distribution for thermalized  $\mu\text{p}$  atoms (atoms which do not undergo the laser excitation) is also shown in the figure illustrating a clear separation in terms of kinetic energy for the two classes of  $\mu\text{p}$  atoms: the ones which simply thermalize, and the ones which undergo a laser excitation.

Because the cross section  $\sigma_{00}$  decreases with increasing energy, the additional energy kick won by the  $\mu\text{p}$  atoms after a successful laser excitation allows them to efficiently diffuse in the  $\text{H}_2$  gas. To illustrate this, in Fig. 6 we also plot the mean free path for  $\mu\text{p}$  atoms in the  $\text{H}_2$  gas as a function of the  $\mu\text{p}$  kinetic energy as calculated from Eq. (4). Note that the minimum in the  $\Gamma_{00}$  rates coincides by chance approximately with the energy which is gained in the deexcitation process.

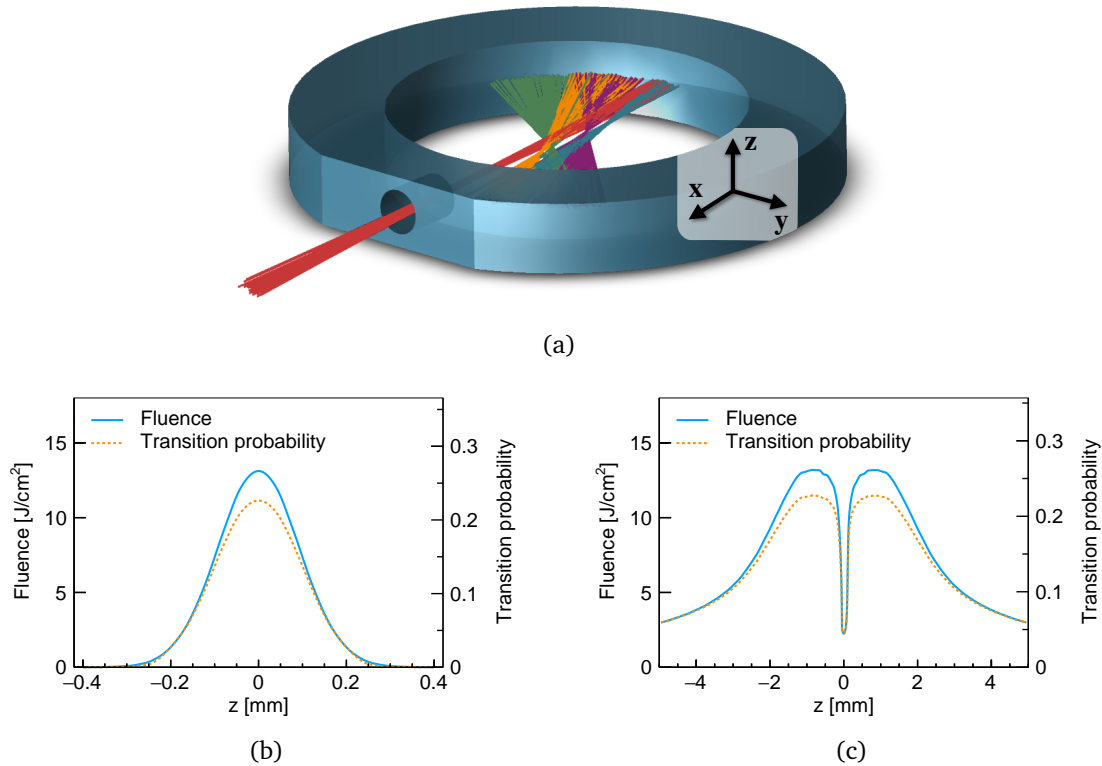


Figure 5: (a) 3D rendering of the toroidal multi-pass cavity with light rays. The laser light is injected into the cavity through a thin slit at a small angle relative to the  $x$ -axis. The light rays bounce back and forth within the cavity. To better illustrate the propagation of the ray bundles in the cavity, at each reflection the color of the rays is changed. (b) Spatial distribution of the fluence along the  $z$ -axis (direction of the muon beam). We assumed an incoupled pulse energy of 1 mJ and a reflectivity of 99.2%. The plotted curve shows the fluence distribution passing through the maximum with a distance of 1 mm from the target center, i.e. with  $x = 1$  mm. The laser-induced transition probability calculated from this fluence for a  $\mu\text{p}$  atom in the  $F = 0$  state sitting in the respective position is also shown assuming additionally a laser bandwidth of 100 MHz, a pulse length of 50 ns, a target temperature of 22 K and a target pressure of 0.6 bar. Saturation effects are visible in the region of maximum fluence. (c) Similar to (b) but in  $x$ -direction, i.e., in radial direction of the multi-pass cavity.

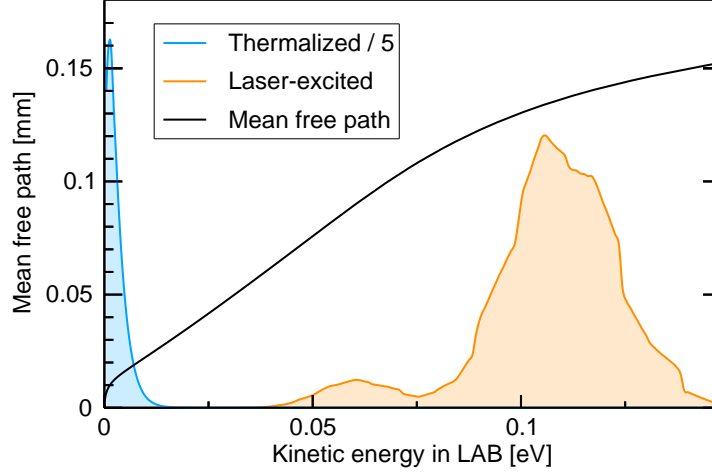


Figure 6: Kinetic energy distributions for thermalised  $\mu\text{p}$  atoms (blue, rescaled in amplitude by a factor of  $1/5$ ) and for  $\mu\text{p}$  atoms right after a successful cycle of laser excitation and collisional quenching from the triplet to the singlet state (orange). The mean free path versus kinetic energy of the  $\mu\text{p}$  atoms is also given. Here we assume a target temperature of 22 K and a pressure of 0.6 bar.

### 6.3 Diffusion after the laser excitation

The  $\mu\text{p}$  atoms with extra kinetic energy from a successful laser excitation are generated in the central region of the target (around the target mid-plate at  $z = 0$ ). Their initial position distribution in  $z$ -direction is given by the excitation curve of Fig. 5b multiplied by the spatial distribution of the  $\mu\text{p}$  atoms at the moment of the laser excitation given in Fig. 4d. Due to their relatively elevated kinetic energy after the collisional quenching and the small collision rate  $\Gamma_{00}$ , these  $\mu\text{p}$  atoms travel comparably long distances and have a probability of reaching one of the target walls before thermalizing again of around 30% at optimal target conditions ( $\varphi = 0.008 - 0.01$ ,  $p = 0.5 - 0.6$  bar,  $T = 22$  K,  $d = 1.0$  mm).

As can be read from the black curve of Fig. 6, the  $\mu\text{p}$  atoms with the 0.1 eV kinetic energy can travel a distance of about 0.1 mm before undergoing a collision. Yet, because the differential cross section is highest for small angles, a large fraction of these collisions lead to small energy losses and small angular deflections so that the  $\mu\text{p}$  atom can efficiently diffuse for several hundred  $\mu\text{m}$  before thermalizing. Figure 7a shows distributions of the distance travelled by  $\mu\text{p}$  atoms in  $\text{H}_2$  gas at 22 K and 0.6 bar ( $\varphi = 0.01$ ) at various times assuming an initial kinetic energy distribution as obtained from the collisional deexcitation of the triplet state (see Fig. 6). For comparison, the distance travelled by thermalized  $\mu\text{p}$  atoms is also given. As can be seen from this figure, within a few hundred nanoseconds, the  $\mu\text{p}$  atoms that received the extra kinetic energy from the laser excitation travel distances that are comparable to the target thickness (ranging from 1 to 1.2 mm). On the contrary, the thermalized  $\mu\text{p}$  atoms, i.e.,  $\mu\text{p}$  atoms that do not undergo laser excitation, travel maximally a few 100  $\mu\text{m}$  in the same time. Relevant for the experiment, the average distance the  $\mu\text{p}$  atoms travel in the  $z$ -direction is displayed in Fig. 7b. The saturation visible after a few hundred nanoseconds is because most of the  $\mu\text{p}$  atoms have lost their excess energy.

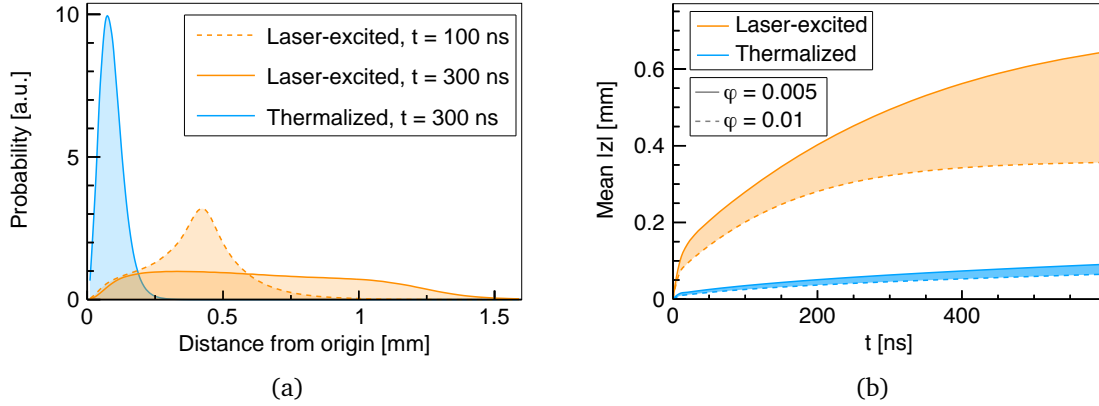


Figure 7: (a) Distance travelled by the  $\mu p$  atoms in the  $H_2$  gas at 22 K temperature and 0.6 bar pressure in 100 and 300 ns, respectively. Two initial kinetic energies were assumed: for thermalized  $\mu p$  atoms (blue) and for  $\mu p$  atoms that have undergone a successful cycle of laser-excitation and collisional quenching (orange) as shown in Fig. 6. (b) Mean distance in  $z$ -direction travelled by the  $\mu p$  atoms as a function of time for two kinetic energy distributions and for two densities.

Figures 8a and 8b show the time distributions of  $\mu p$  atoms reaching one of the walls, assuming that the laser pulses are coupled into the multi-pass cavity at time  $t = 1000$  ns and that the  $\mu p$  atoms are formed at time  $t = 0$ . These simulations use the results from the diffusion simulation prior to the laser excitation and the results from the laser excitation section. In both cases we assumed the 50/50 distribution for the initial  $\mu p$  energy and we simulated a target with 0.6 bar pressure and 22 K temperature. Only the target thickness differentiates the two simulations: for the left plot we used a thickness of  $d = 1.0$  mm, for the right plot we used a thickness of  $d = 1.2$  mm. Each plot shows two curves: the orange curves represent the distribution of arrival times for  $\mu p$  atoms that have undergone the laser excitation, while the blue curves represent the arrival times for all  $\mu p$  atoms independently of whether or not they have undergone the laser excitation. As visible from the orange curves, it takes about 100 ns until the first  $\mu p$  atoms which have undergone laser excitation reach one of the target walls. Most of them however arrive at the walls in a time window spanning from about 1100 to 1500 ns (that depends on the target thickness). This spread of arrival times originates from the initial kinetic energy distribution, the isotropic distribution of the initial velocity, the spatial distribution of the  $\mu p$  atoms at the time of the laser excitation and the collisional effects during the diffusion process.

By considering the blue curves of Figs. 8a and 8b, we notice that there is a large fraction of  $\mu p$  atoms arriving at the target walls without being excited by the laser pulse. These  $\mu p$  atoms give rise to background events as each  $\mu p$  atom arriving at the target walls leads to a  $\mu Au$  event, independently of whether previously they had undergone or not a laser excitation. This background is produced by  $\mu p$  atoms that have thermalized in the vicinity of the target walls and that slowly diffuse to one of the walls in the event time window within which laser-induced  $\mu Au$  events are recorded.

The simulations of Figs. 8a and 8b are normalized by the number of incident muons and account for the stopping probability in the hydrogen gas,  $P_{\text{stop}}$ , which was estimated conservatively

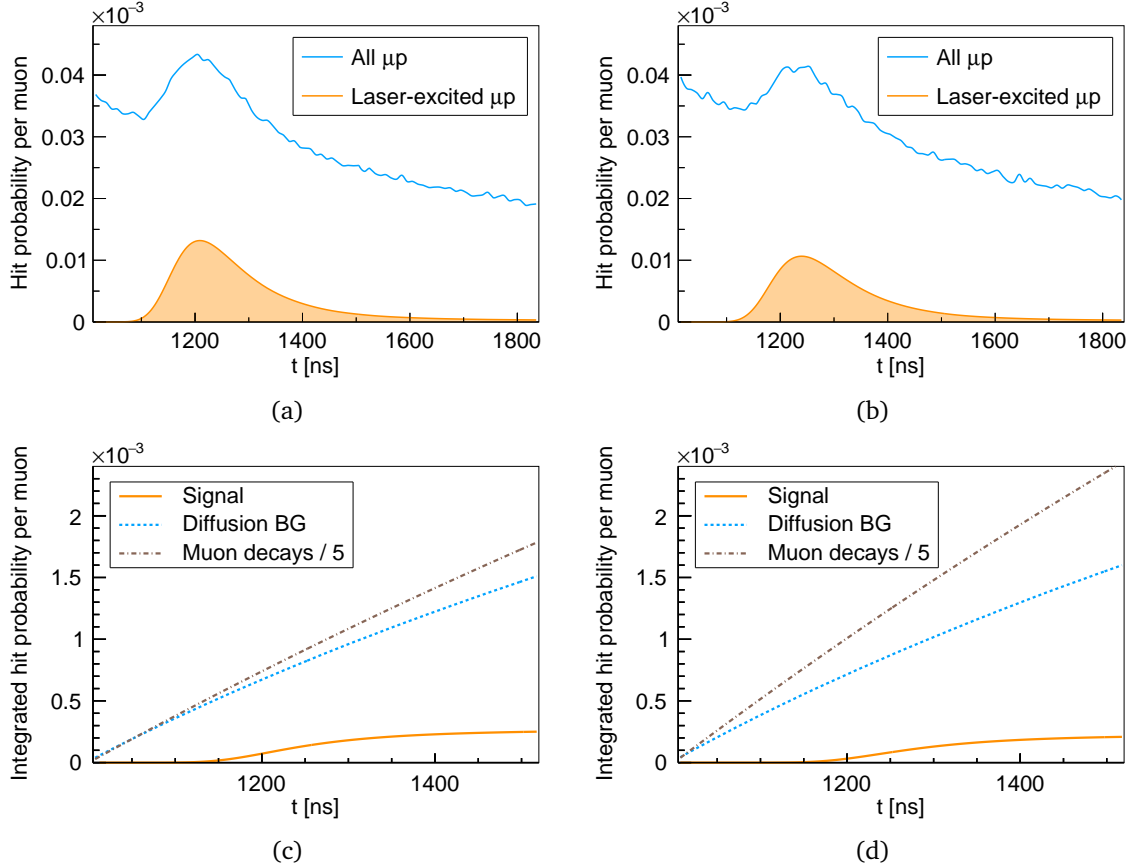


Figure 8: (a) Time distribution of the  $\mu p$  atoms arriving at one of the target walls for times following the laser excitation. In orange we show the arrival times only for  $\mu p$  atoms that have undergone laser excitation, in blue for all  $\mu p$  atoms. We assume the 50/50 initial  $\mu p$  energy distribution described in Sec. 5 and a hydrogen gas target with 22 K temperature, 0.6 bar pressure and 1.0 mm thickness. We further assume that at  $t = 1000$  ns, laser pulses of 1 mJ energy, 50 ns pulse length and 100 MHz bandwidth are coupled into the multi-pass cavity having a reflectivity of 99.2%. The hit probabilities have been normalized to the number of muons entering the target and binned in 10 ns. (b) Similar to (a) but for a target thickness of 1.2 mm. (c) and (d) Integral from 1000 ns to  $t$  of the time spectra depicted in Figs. 8a and 8b, respectively. The dark brown (dashed-dotted) curves represent the probability per entering muon that a  $\mu p$  atom is decaying in the time window between 1000 ns and  $t$ . Note that this probability has been divided by 5 to increase readability.



based on measurements using the relation

$$P_{\text{stop}}[\%] = 500 \cdot \frac{p [\text{bar}] \cdot d [\text{mm}]}{T [\text{K}]}, \quad (5)$$

where  $T$  is the temperature of the gas in K,  $p$  the target pressure in bar, and  $d$  the target thickness in mm.

The time window in which the  $\mu\text{Au}$  events have to be searched for (event time window), has to be selected as a trade-off between signal and background rates. Figures 8c and 8d represent the integral from 1000 ns to  $t$  of the time spectra depicted in Figs. 8a and 8b, respectively. Hence, the asymptotic value of the orange curves of Figs. 8c and 8d represents the probability for a laser-induced  $\mu\text{Au}$  event per entering muon. As we will see in the next section, these integrals allow to quickly determine signal and background rates in a given event time window. On top of the above described diffusion-related background visible in Figs. 8a and 8b, there are two other sources of background that we have to consider in the spectroscopy experiment. One is a muon-uncorrelated background, i.e., a background originating from natural radioactivity in the experimental area, from neutrons produced by the accelerator facility, from possible electron contamination of the muon beam and from cosmic muons. The other and more important background originates from false identifications of muon decays as  $\mu\text{Au}$  events. The dark brown (dashed-dotted) curves in Fig. 8c and 8d represent the integral number of muon decays occurring between 1000 ns and the time  $t$ . Even in the optimal event time window there is one order of magnitude more muon decays than laser-induced  $\mu\text{Au}$  events (note that these curves have been scaled by a factor of five to ease the representation). To mitigate this possible background source, the detection system has to minimise the false identification of muon decay events as  $\mu\text{Au}$  events, while maximising the detection probability for  $\mu\text{Au}$  events.

## 7 Signal and background rates and target optimization

In this section we first summarize how the simulation of the diffusion process can be used to estimate the signal and background rates of the HFS experiment. The target pressure, temperature and length are then optimized such that the largest statistical significance is reached.

The signal rate  $R_{\text{signal}}$  can be estimated using

$$\begin{aligned} R_{\text{signal}} &= P_{\text{signal}} \cdot R_{\mu} \cdot \varepsilon_{\text{Au}} \\ &= 2.5 \times 10^{-4} \cdot 500 [1/\text{s}] \cdot 0.7 = 0.088 \text{ 1/s}, \end{aligned} \quad (6)$$

where  $R_{\mu} = 500 \text{ 1/s}$  is the muon trigger rate in the entrance detector (limited by the laser repetition rate) and  $\varepsilon_{\text{Au}}$  is the detection efficiency for a  $\mu\text{Au}$  event. We use here a conservative value of  $\varepsilon_{\text{Au}} = 0.7$  as measured with a prototype detection system [40].  $P_{\text{signal}}$  is the probability that a muon passing the entrance detector eventually produces a  $\mu\text{Au}$  atom that reaches one of the target walls in the event time window after undergoing a laser-excitation. This value can be extracted from the orange curves of Fig. 8c and Fig. 8d considering the difference between beginning and end of the event time window. For an event time window spanning from 1.1 to 1.5  $\mu\text{s}$ , we obtain  $P_{\text{signal}} = 2.5 \times 10^{-4}$  when assuming an in-coupled pulse energy of 1 mJ, a cavity reflectivity of 99.2%, a laser bandwidth of 100 MHz, and a target with 0.6 bar pressure, 22 K temperature, 1 mm thickness and 15 mm diameter.

The rate of the diffusion-related background (see Fig. 8a and Fig. 8b) is given by

$$\begin{aligned} R_{\text{BG}}^{\text{diffusion}} &= P_{\text{diffusion}} \cdot R_{\mu} \cdot \varepsilon_{\text{Au}} \\ &= 11.1 \times 10^{-4} \cdot 500 \text{ 1/s} \cdot 0.7 = 0.39 \text{ 1/s}, \end{aligned} \quad (7)$$

where  $P_{\text{diffusion}}$  is the probability that a muon passing the entrance detector diffuses in the hydrogen gas and hits a target wall in the event time window. This value can be extracted from the blue curves of Fig. 8c and Fig. 8d considering the difference between the beginning and end of the event time window.

The background rate caused by muon decay is given by

$$\begin{aligned} R_{\text{BG}}^{\text{decay}} &= P_{\text{decay}} \cdot R_{\mu} \cdot \varepsilon_{\text{Au-false}} \\ &= 67.5 \times 10^{-4} \cdot 500 \text{ 1/s} \cdot 0.09 = 0.30 \text{ 1/s}, \end{aligned} \quad (8)$$

where  $P_{\text{decay}}$  is the probability that a muon entering the target decays in the event time window.  $P_{\text{decay}}$  can be extracted from the dark brown (dashed-dotted) curves of Fig. 8c and Fig. 8d.  $\varepsilon_{\text{Au-false}}$  is the probability that an electron from a muon decay is falsely identified in the detection system as a  $\mu\text{Au}$  event. This false identification arises mainly from decay electrons producing Bremsstrahlung when passing the target mechanics and the optical cavity. In a test beamtime, using a detection system prototype with a realistic material budget we measured  $\varepsilon_{\text{Au-false}} = 0.09$  [40].

Accidental energy depositions in the event time window are responsible for a third type of background. These energy depositions are mainly produced by the natural radioactivity present in the experimental area, and by neutrons produced by the accelerator complex. Based on the measured accidental rate in the x-ray detection system [40], we predict an accidental background rate in the spectroscopy experiment of  $R_{\text{BG}}^{\text{accidental}} = 0.2 \text{ 1/s}$  for a muon rate of  $R_{\mu} = 500 \text{ 1/s}$  and a 400 ns wide event time window (which determines the duration of the exposure to the accidental background).

The signal and background rates have been computed for various target conditions and the results are summarized in Table 1. The target conditions have been varied to find the maximum of the ratio  $R_{\text{signal}}/\sqrt{R_{\text{BG}}}$ , where  $R_{\text{BG}} = R_{\text{BG}}^{\text{diffusion}} + R_{\text{BG}}^{\text{decay}} + R_{\text{BG}}^{\text{accidental}}$  is the total background rate. Maximizing this ratio is equivalent to maximizing the statistical significance and minimizing the time needed to expose the signal over the statistical fluctuations of the background. Hence, in Table 1 we also list the average time needed to observe the signal with a  $4\sigma$  significance over the background, which is calculated from the rates using

$$t_{4\sigma} = 16 \frac{R_{\text{BG}}}{R_{\text{signal}}^2}. \quad (9)$$

In the following, we use this time  $t_{4\sigma}$  as a figure of merit to find the optimal target conditions, and to estimate the maximum time needed to search for the resonance. The pressure dependence of  $t_{4\sigma}$  is shown in Fig. 9 for a constant target temperature of 22 K, for two laser bandwidths, and two target thicknesses. In this parameter range, the minimum is reached for pressures around 0.5 bar, which motivates the pressure choice in Table 1. Temperatures lower than 22 K would lead in principle to shorter  $t_{4\sigma}$  times (smaller  $R_{\text{BG}}^{\text{diffusion}}$  and larger laser transition probability), but are excluded to avoid liquefaction of the  $\text{H}_2$  gas. Target lengths slightly smaller than 1 mm would also lead to smaller  $t_{4\sigma}$ , but this would also cause larger diffraction losses for the laser light passing the region between the two target walls. This effect cannot be easily quantified as it is strongly dependent on the relative alignment between the laser beam and multi-pass cavity. For

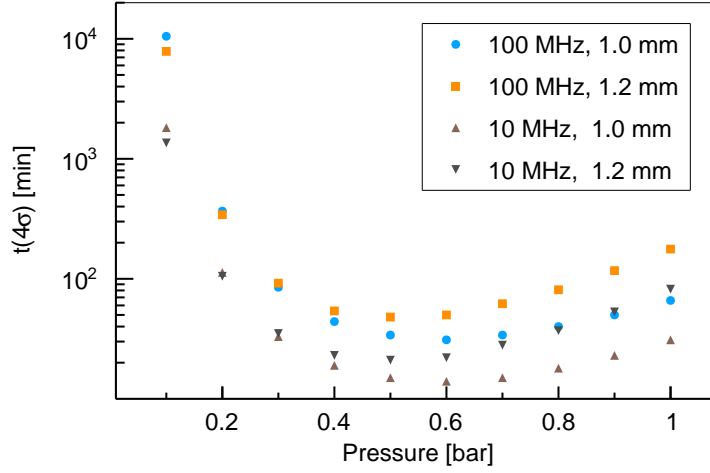


Figure 9: Average time  $t_{4\sigma}$  needed to observe the signal with a significance over background of  $4\sigma$  as a function of the  $\text{H}_2$  gas pressure for two target thicknesses ( $d = 1.0$  mm and  $d = 1.2$  mm) and two laser bandwidths (100 MHz and 10 MHz).

Table 1: Signal rates, background rates and  $t_{4\sigma}$  for two different pressures  $p$ , two target thicknesses  $d$  and two laser bandwidths  $\Delta_l$ . We use  $R_\mu = 500$  1/s,  $\varepsilon_{\text{Au}} = 0.7$ , and  $\varepsilon_{\text{Au-false}} = 0.09$ . Above the horizontal line we used the 50/50 distribution of the initial  $\mu\text{p}$  energy. Below the line we assumed that all the  $\mu\text{p}$  atoms have an initial kinetic energy of 100 eV. To compute the signal rates we further assume that the laser is on resonance, with an in-coupled pulse energy of 1.0 mJ, a cavity reflectivity of 99.2% and a pulse length of 50 ns.

$\Delta_l$ [MHz]	$d$ [mm]	$p$ [bar]	$R_{\text{Signal}}$ [1/s]	$R_{\text{BG}}^{\text{diffusion}}$ [1/s]	$R_{\text{BG}}^{\text{decay}}$ [1/s]	$R_{\text{BG}}^{\text{accidental}}$ [1/s]	$R_{\text{Signal}}/R_{\text{BG}}$	$t_{4\sigma}$ [min]
100	1.0	0.5	7.7e-02	3.2e-01	2.2e-01	0.2	1.0e-01	34
100	1.0	0.6	8.8e-02	3.9e-01	3.0e-01	0.2	9.8e-02	31
100	1.2	0.5	7.0e-02	3.5e-01	3.1e-01	0.2	8.1e-02	48
100	1.2	0.6	7.4e-02	4.1e-01	4.1e-01	0.2	7.3e-02	50
10	1.0	0.5	1.2e-01	3.2e-01	2.2e-01	0.2	1.6e-01	15
10	1.0	0.6	1.3e-01	3.9e-01	3.0e-01	0.2	1.5e-01	14
10	1.2	0.5	1.1e-01	3.5e-01	3.1e-01	0.2	1.2e-01	21
10	1.2	0.6	1.1e-01	4.1e-01	4.1e-01	0.2	1.1e-01	22
100	1.0	0.5	5.9e-02	2.4e-01	1.7e-01	0.2	9.7e-02	47
100	1.0	0.6	7.1e-02	3.0e-01	2.4e-01	0.2	9.5e-02	40
100	1.2	0.5	5.7e-02	2.7e-01	2.5e-01	0.2	7.9e-02	60
100	1.2	0.6	6.3e-02	3.3e-01	3.5e-01	0.2	7.2e-02	59
10	1.0	0.5	8.9e-02	2.4e-01	1.7e-01	0.2	1.5e-01	21
10	1.0	0.6	1.1e-01	3.0e-01	2.4e-01	0.2	1.4e-01	18
10	1.2	0.5	8.6e-02	2.7e-01	2.5e-01	0.2	1.2e-01	26
10	1.2	0.6	9.6e-02	3.3e-01	3.5e-01	0.2	1.1e-01	26

this reason, in this study we assume that the minimal possible target length is  $d = 1$  mm and for the conservative estimates we use  $d = 1.2$  mm.

To study the sensitivity of the results to the initial kinetic energy of the  $\mu\text{p}$  atoms, in Table 1 we list rates and  $t_{4\sigma}$  values for the two different models of the initial kinetic energy of the  $\mu\text{p}$  atoms as described in Sec. 5. Using the most conservative assumption of the initial kinetic energies (all  $\mu\text{p}$  at 100 eV energy) instead of the 50/50 distribution,  $t_{4\sigma}$  is increased by 20 to 40 % depending on the other parameters.

As can be seen from Table 1, for the most conservative estimate of the performance we obtain  $t_{4\sigma} \approx 60$  min. This can be considerably improved by decreasing the target length or the laser bandwidth. In addition, note that  $t_{4\sigma}$  is inversely proportional to the square of the laser energy and the cavity lifetime, such that an improvement of the performance of the laser system and the multi-pass cavity can significantly decrease  $t_{4\sigma}$ .

## 8 Search and scan of the HFS resonance

In this section we first roughly estimate the maximum time needed to search for the resonance and then we calculate the statistical accuracy with which the resonance frequency can be determined. For both cases, we need to assume a certain performance of the experimental setup and to use the simulation of the diffusion process presented above.

The HFS resonance, which has a linewidth of about 230 MHz at FWHM [17], has to be searched for in a region of about 40 GHz corresponding to a  $\pm 3\sigma$  band of the present theory uncertainty given mainly by the uncertainty of the two-photon exchange contribution [5, 7, 9–12, 21, 22]. An efficient search of the resonance has to be accomplished in steps of about 100 MHz corresponding to about 0.5 FWHM, such that the maximum number of frequency points that needs to be measured is about 400. A recent evaluation of the two-photon exchange contribution in muonic hydrogen [5] that uses the two-photon exchange contribution extracted from regular hydrogen has decreased its uncertainty by a factor of two. However, we still conservatively assume a 40 GHz wide search region.

The resonance will be searched for by counting the number of x rays for a time of  $1.4t_{4\sigma}$  at a given laser frequency. Then the laser frequency is shifted by 100 MHz and the x-ray counting is performed anew. This is repeated until a statistically significant deviation of the number of x rays above the background level is observed. The factor of 1.4 multiplying  $t_{4\sigma}$  takes into account that, while searching for the resonance, none of the chosen frequency points necessarily matches the resonance maximum. As the maximum deviation from resonance is 50 MHz (for 100 MHz frequency steps) the maximum decrease of the laser-induced transition probability is 0.86, resulting in an increase of the time needed to see the signal over background by a factor of  $1/0.86^2 = 1.4$ .

This procedure to search for the resonance has been validated by simulating the search for the resonance  $10^5$  times. The number of events at each frequency point (spaced by 100 MHz) is generated according to a Poissonian distribution with expectation values derived from the signal and background rates given in Table 1 and accounting for the wavelength dependence of the signal rate according to Ref. [17]. One of these simulations is shown in Fig. 10 (a). As visible in this figure, the maximum of the counts has been found at the frequency which is nearest to the resonance position  $\nu_0$  used to generate the pseudo-data.

By considering the simulated resonance searches, we found that for 97.43 % of the cases, the maximum of the simulated pseudo-data has been found in correspondence of the resonance (see

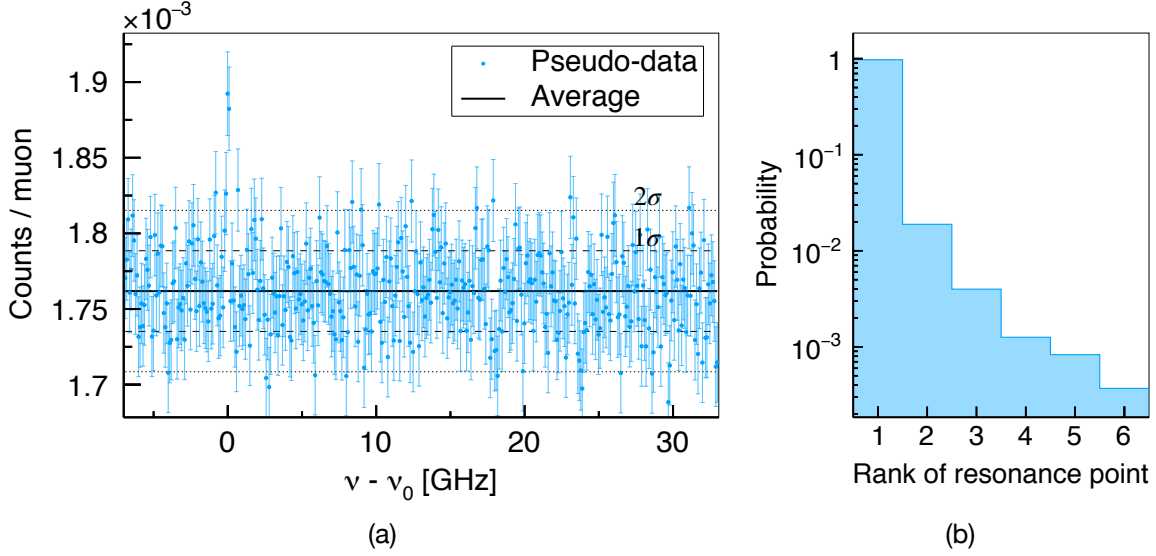


Figure 10: (a) Simulation of the resonance search in which a time  $1.4t_{4\sigma}$  is spent at each frequency point.  $\nu$  denotes the laser frequency,  $\nu_0$  the resonance frequency. (b) Ranking of the frequency points in correspondence of the resonance. For 97.43 % of the cases the simulated pseudo-data have a maximum in correspondence of the resonance. For 1.84 % of the cases the second largest point is in correspondence of the resonance and so on.

Fig. 10 (b)). As can be seen from the same figure, the probability that only the second highest point is at the position of the resonance is about 1.84 % and the probability that only the third highest point is at the position of the resonance is 0.39 %. Summing up these probabilities, we obtain 99.66 %, which corresponds to the probability of identifying the position of the resonance by adding additional measurement time to the three points with the largest amplitude. Hence, we confirm that the above described simple procedure to search for the resonance with 100 MHz steps and by accumulating statistics at each frequency point for a time of  $1.4t_{4\sigma}$  is adequate.

The maximum time needed to search for the resonance (using the simple procedure described above) can be estimated to be  $400 \times (1.4t_{4\sigma} + t_{\lambda\text{-change}}) \frac{1}{\epsilon_{\text{uptime}}} = 82'300$  minutes, corresponding to 8.2 weeks. For this estimate, we have used conservative values for the experimental performance: an uptime (including accelerator) of  $\epsilon_{\text{uptime}} = 70\%$ , a time  $t_{\lambda\text{-change}} = 1$  h to change the laser frequency, a laser pulse energy of 1 mJ, a laser bandwidth of 100 MHz, a cavity reflectivity of 99.2 %, a muon rate of 500 1/s,  $\epsilon_{\text{Au}} = 0.7$ ,  $\epsilon_{\text{Au-false}} = 0.09$ , a target thickness of 1.2 mm, and scan range of 40 GHz. Moreover, we assumed that all  $\mu\text{p}$  atoms have 100 eV initial kinetic energy. Most probably the resonance can be found much faster if a significant deviation from background is found earlier and by adapting the search strategy (i.e. accumulating more statistics on points with significant deviations from background).

We have also simulated  $10^5$  pseudo-measurements of the HFS resonance after its discovery, assuming that two weeks of beamtime can be used to measure the resonance (this time does not include the time needed to change the laser wavelength and the time when the setup or the accelerator are not operating). A simulation of a resonance measurement for conservative assumptions is shown in Fig. 11a. Figure 11b shows a similar simulation for slightly less conservative assump-

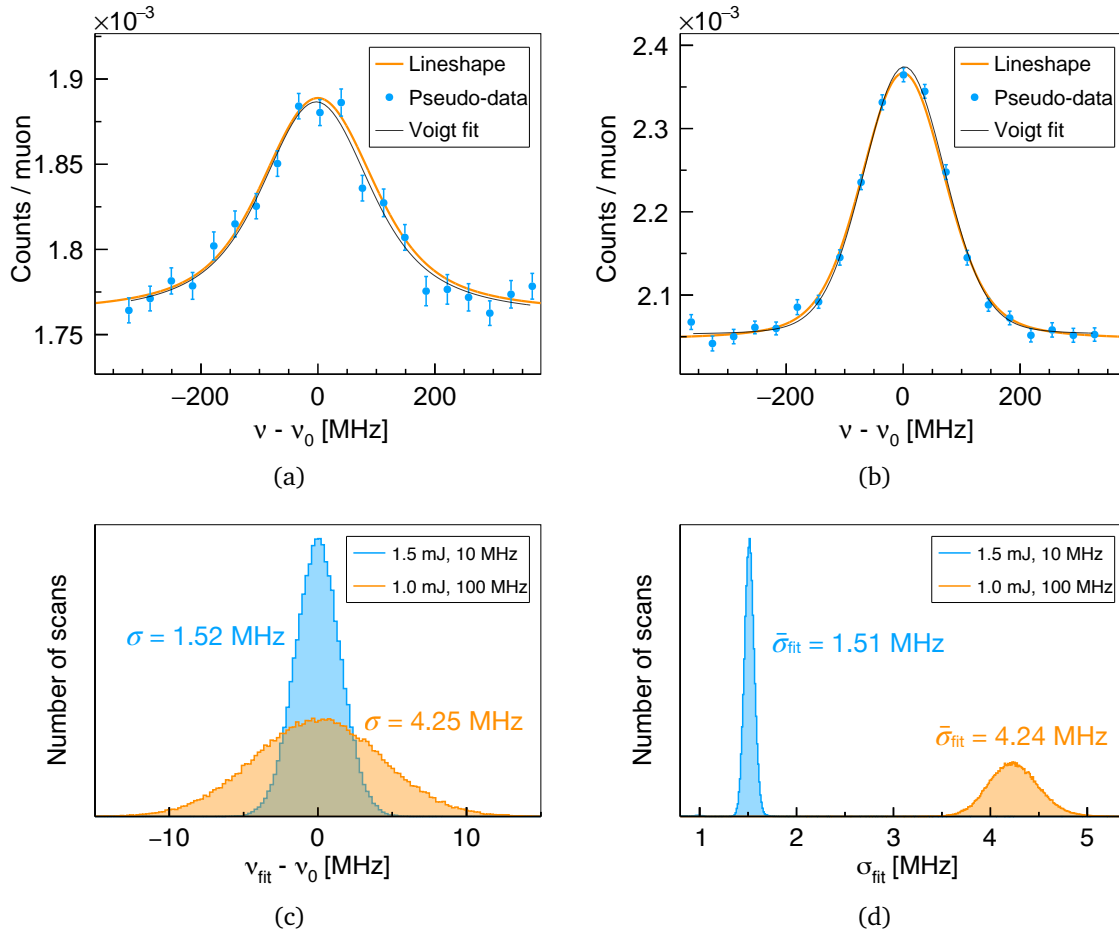


Figure 11: (a) Simulated pseudo-measurement of the HFS transition for two weeks of measurement. We assumed here an initial  $\mu\text{p}$  energy of 100 eV, a laser pulse energy of 1 mJ, a laser bandwidth of 100 MHz, a cavity reflectivity of 99.2%, a muon rate of 500 1/s,  $\epsilon_{\text{Au}} = 0.7$ ,  $\epsilon_{\text{Au-false}} = 0.09$ , a target thickness of 1.2 mm and an accidental rate of 0.2 1/s. (b) Similar to (a) but for a pulse energy of 1.5 mJ, a laser bandwidth of 10 MHz and the more realistic initial kinetic energy distribution as presented in Sec. 5. (c) Distribution of the bias obtained by fitting a Voigt function to the resonance data for  $10^5$  pseudo-measurements. The orange distribution has been obtained from data generated at the conditions used in (a), the blue distribution from data generated at the conditions used in (b). (d) Fit uncertainties of the centroid position obtained from the fits discussed in (c).

tions to highlight the potential of the experimental scheme. In both cases we have chosen regular frequency steps of 35 MHz and we have distributed a similar amount of time to each frequency point with maximum fluctuation of about 20 %. Hence, we did not put any effort into optimizing the distribution of the available time at the various laser frequencies.

The obtained pseudo-experiments were then fit using a Voigt function to determine the centroid positions. The results from the fits are given in Figs. 11c and 11d. Figure 11c shows the bias, i.e., the difference between fitted positions and actual position assumed when generating the pseudo-data. Its distribution is Gaussian centered at zero with  $\sigma = 4.25$  MHz and  $\sigma = 1.52$  MHz, for the most conservative and less conservative assumptions of the experimental performance used to generate Figs. 11a and 11b, respectively. Figure 11d gives the distributions of the fit uncertainties of the centroid position. The results are equivalent to the standard deviation of the bias, demonstrating that fitting with a simple Voigt profile is adequate.

From these plots, we can thus conclude that a statistical uncertainty of a few MHz can be reached for the HFS spectroscopy experiment even with the most conservative assumptions of the setup performance. This corresponds to a relative accuracy of about 0.1 ppm to be compared with the goal of 1 ppm. Hence, even assuming a conservative performance of the experimental setup, it should be possible to find and measure the resonance with relative accuracies below the ppm level within a beamtime having a duration less than 12 weeks which is approximately the maximum time that can be allocated at the PSI CHRISP facility.

## 9 Conclusion

In this paper we presented simulations of the diffusion of  $\mu\text{p}$  atoms in the hydrogen gas prior and after the laser excitation to optimize the hydrogen target conditions, to estimate signal and background rates and to assess the statistical uncertainty of the HFS experiment. The simulations were implemented into Geant4 using double-differential collision rates for the scattering between  $\mu\text{p}$  in the ground state and  $\text{H}_2$  molecules. Possible excitation of the  $\text{H}_2$  molecules and transitions of the  $\mu\text{p}$  atom between the singlet and triplet sub-levels are accounted for. Because the kinetic energy of the hydrogen molecules can not be neglected compared with the kinetic energy of the  $\mu\text{p}$  atoms, we accounted also for the initial kinetic energy of the  $\text{H}_2$  molecules. This has been obtained by calculating the double differential collision rates averaged over the distribution of velocities of the hydrogen molecules as given in Eq. (3). In this way, the Geant4 simulations were capable to include, in an effective way, the  $\text{H}_2$  motion and thus the gas target temperature. We applied a similar code with similar cross sections to quantify the diffusion of muonic deuterium in a high pressure  $\text{H}_2$  gas cell in the context of the muX experiment and we found good agreement between simulation and measurements [41].

In the presented simulations we have used a conservative approximation of the initial kinetic energy (after the  $\mu\text{p}$  atom formation and deexcitation) derived from the results of the cascade model presented in Ref. [35] for  $\varphi = 0.015$  and modified to account for the fact that the  $\mu\text{p}\text{-H}_2$  cross sections are available only up to 100 eV. By considering the extreme case that all  $\mu\text{p}$  atoms after the deexcitation would have 100 eV kinetic energy, we have investigated the sensitivity of the results to the initial kinetic energy and derived lower bounds for the signal and background rates.

With the diffusion simulations we computed the processes that lead to a signal event and the two main backgrounds. Combined with the measured values for the detection efficiencies

$\varepsilon_{\text{Au}} = 0.7$  and  $\varepsilon_{\text{Au-false}} = 0.09$ , we were able to estimate signal and background rates. We optimized the target conditions using the ratio  $R_{\text{signal}}/\sqrt{R_{\text{BG}}}$  as a figure of merit and we found that the optimal pressure is between 0.5 and 0.6 bar for target temperatures of 22 K (corresponding to  $\varphi = 0.008 - 0.01$ ) and target thicknesses between 1 and 1.2 mm. Lower temperatures are not possible as the hydrogen gas liquefies, while target lengths smaller than 1 mm would lead to diffraction losses of the laser beam.

Using these optimized target conditions (0.6 bar and 22 K) and conservative estimates of the other still unknown parameters (1 mJ in-coupled laser pulse energy, a cavity reflectivity of 99.2%, a laser bandwidth of 100 MHz and 1.2 mm target thickness) we have estimated the maximum time needed to search for the resonance. Nine weeks of beam time should be sufficient to find the resonance even when the resonance has to be searched in a 40 GHz wide region. With additional two weeks of data taking (corresponding to three weeks of beam time), it is possible to measure the HFS transition with sub ppm statistical uncertainty. Turning around the point of view, these simulations allow to precisely define the requirements for the experimental setup.

## Acknowledgments

We acknowledge the support of the following grants: FCT - Fundação para a Ciência e a Tecnologia (Portugal) through national funds in the frame of projects PTDC/FIS-AQM/29611/2017 and UID/04559/2020 (LIBPhys); Deutsche Forschungsgemeinschaft (DFG, German Research Foundation) under Germany's Excellence Initiative EXC 1098 PRISMA (194673446), Excellence Strategy EXC PRISMA+ (390831469) and DFG/ANR Project LASIMUS (DFG Grant Agreement 407008443); The French National Research Agency with project ANR-18-CE92-0030-02; The European Research Council (ERC) through CoG. #725039, and the Swiss National Science Foundation through the projects SNF 200021\_165854 and SNF 200020\_197052.

## References

- [1] R. Pohl *et al.*, *The size of the proton*, Nature **466**, 213 (2010), doi:[10.1038/nature09250](https://doi.org/10.1038/nature09250).
- [2] A. Antognini *et al.*, *Proton Structure from the Measurement of 2S – 2P Transition Frequencies of Muonic Hydrogen*, Science **339**, 417 (2013), doi:[10.1126/science.1230016](https://doi.org/10.1126/science.1230016).
- [3] R. Pohl *et al.*, *Laser spectroscopy of muonic deuterium*, Science **353**(6300), 669 (2016), doi:[10.1126/science.aaf2468](https://doi.org/10.1126/science.aaf2468).
- [4] J. J. Krauth *et al.*, *Measuring the  $\alpha$ -particle charge radius with muonic helium-4 ions*, Nature **589**(7843), 527 (2021), doi:[10.1038/s41586-021-03183-1](https://doi.org/10.1038/s41586-021-03183-1).
- [5] A. Antognini, F. Hagelstein and V. Pascalutsa, *The Proton Structure in and out of Muonic Hydrogen*, Annual Review of Nuclear and Particle Science **72**(1), 389 (2022), doi:[10.1146/annurev-nucl-101920-024709](https://doi.org/10.1146/annurev-nucl-101920-024709).
- [6] C. Peset, A. Pineda and O. Tomalak, *The proton radius (puzzle?) and its relatives*, Prog. Part. Nucl. Phys. **121**, 103901 (2021), doi:[10.1016/j.pnpnp.2021.103901](https://doi.org/10.1016/j.pnpnp.2021.103901).



- [7] C. Peset and A. Pineda, *Model-independent determination of the two-photon exchange contribution to hyperfine splitting in muonic hydrogen*, JHEP **04**, 060 (2017), doi:[10.1007/JHEP04\(2017\)060](https://doi.org/10.1007/JHEP04(2017)060).
- [8] C. Peset and A. Pineda, *The two-photon exchange contribution to muonic hydrogen from chiral perturbation theory*, Nucl. Phys. B **887**, 69 (2014), doi:[10.1016/j.nuclphysb.2014.07.027](https://doi.org/10.1016/j.nuclphysb.2014.07.027).
- [9] F. Hagelstein, R. Miskimen and V. Pascalutsa, *Nucleon Polarizabilities: from Compton Scattering to Hydrogen Atom*, Prog. Part. Nucl. Phys. **88**, 29 (2016), doi:[10.1016/j.pnpnp.2015.12.001](https://doi.org/10.1016/j.pnpnp.2015.12.001).
- [10] F. Hagelstein and V. Pascalutsa, *Proton structure in the hyperfine splitting of muonic hydrogen*, PoS **CD15**, 077 (2016), doi:[10.22323/1.253.0077](https://doi.org/10.22323/1.253.0077).
- [11] C. E. Carlson, V. Nazaryan and K. Griffioen, *Proton structure corrections to hyperfine splitting in muonic hydrogen*, Phys. Rev. A **83**, 042509 (2011), doi:[10.1103/PhysRevA.83.042509](https://doi.org/10.1103/PhysRevA.83.042509).
- [12] O. Tomalak, *Two-Photon Exchange Correction to the Lamb Shift and Hyperfine Splitting of S Levels*, Eur. Phys. J. A **55**(5), 64 (2019), doi:[10.1140/epja/i2019-12743-1](https://doi.org/10.1140/epja/i2019-12743-1).
- [13] S. G. Karshenboim, *Model-independent determination of the magnetic radius of the proton from spectroscopy of ordinary and muonic hydrogen*, Phys. Rev. D **90**(5), 053013 (2014), doi:[10.1103/PhysRevD.90.053013](https://doi.org/10.1103/PhysRevD.90.053013).
- [14] R. N. Faustov, A. P. Martynenko, F. A. Martynenko and V. V. Sorokin, *Nuclear radiative recoil corrections to the hyperfine structure of S-states in muonic hydrogen*, Phys. Part. Nucl. **48**(5), 819 (2017), doi:[10.1134/S106377961705015X](https://doi.org/10.1134/S106377961705015X).
- [15] A. Antognini, Y.-H. Lin and U.-G. Meißner, *Precision calculation of the recoil–finite-size correction for the hyperfine splitting in muonic and electronic hydrogen* (2022), [arxiv:2208.04025](https://arxiv.org/abs/2208.04025).
- [16] C. Pizzolotto *et al.*, *The FAMU experiment: muonic hydrogen high precision spectroscopy studies*, Eur. Phys. J. A **56**(7), 185 (2020), doi:[10.1140/epja/s10050-020-00195-9](https://doi.org/10.1140/epja/s10050-020-00195-9).
- [17] P. Amaro *et al.*, *Laser excitation of the 1s-hyperfine transition in muonic hydrogen*, SciPost Phys. **13**, 020 (2022), doi:[10.21468/SciPostPhys.13.2.020](https://doi.org/10.21468/SciPostPhys.13.2.020).
- [18] M. Sato *et al.*, *Laser spectroscopy of the hyperfine splitting energy in the ground state of muonic hydrogen*, In *Proceedings, 20th International Conference on Particles and Nuclei (PANIC 14), Hamburg, Germany, August 24-29, 2014*, doi:[10.3204/DESY-PROC-2014-04/67](https://doi.org/10.3204/DESY-PROC-2014-04/67) (2014).
- [19] A. Dupays, A. Beswick, B. Lepetit, C. Rizzo and D. Bakalov, *Proton Zemach radius from measurements of the hyperfine splitting of hydrogen and muonic hydrogen*, Phys. Rev. A **68**, 052503 (2003), doi:[10.1103/PhysRevA.68.052503](https://doi.org/10.1103/PhysRevA.68.052503).
- [20] K. Pachucki, *Theory of the Lamb shift in muonic hydrogen*, Phys. Rev. A **53**, 2092 (1996), doi:[10.1103/PhysRevA.53.2092](https://doi.org/10.1103/PhysRevA.53.2092).
- [21] F. Hagelstein,  *$\Delta(1232)$ -Resonance in the Hydrogen Spectrum*, Few Body Syst. **59**(5), 93 (2018), doi:[10.1007/s00601-018-1403-x](https://doi.org/10.1007/s00601-018-1403-x).

- [22] R. Faustov, I. Gorbacheva and A. Martynenko, *Proton polarizability effect in the hyperfine splitting of the hydrogen atom*, Proc. SPIE Int. Soc. Opt. Eng. **6165**, 0M (2006), doi:[10.1117/12.696903](https://doi.org/10.1117/12.696903).
- [23] J. Nuber, *Doctoral Thesis*, ETH Zurich (in preparation).
- [24] *The Swiss research infrastructure for particle physics CHRISP*, <https://www.psi.ch/en/media/our-research/the-swiss-research-infrastructure-for-particle-physics-chrisp>.
- [25] S. S. Gershtein, *Transition between hyperfine structure levels in mu-mesic hydrogen*, Sov. Phys. JETP **34**, 463 (1958).
- [26] L. Bracci, C. Chiccoli, G. Fiorentini, V. S. Melezhik, P. Pasini, L. I. Ponomarev and J. Wozniak, *The atlas of the cross sections of mesic atomic process I. The processes  $p\mu + p, d\mu + d$  and  $t\mu + t$* , Muon Catalyzed Fusion **4**, 247 (1989).
- [27] L. Bracci, C. Chiccoli, G. Fiorentini, V. S. Melezhik, P. Pasini and J. Wozniak, *Calculation of the elastic scattering cross sections for  $p\mu + p$  and  $t\mu + t$  collisions in adiabatic representation*, Phys. Lett. A **149**, 463 (1990).
- [28] M. Bubak and M. P. Faifman, *Cross sections for hydrogen muonic atomic processes in two-level approximation of the adiabatic framework*, JINR Preprint E4-87-464 (1987).
- [29] A. Adamczak, M. P. Faifman, L. I. Ponomarev, V. I. Korobov, V. S. Melezhik, R. T. Siegel and J. Woźniak, *Atlas of cross sections for scattering of muonic hydrogen atoms on hydrogen isotope molecules*, At. Data and Nucl. Data Tables **62**, 255 (1996), doi:[10.1006/adnd.1996.0006](https://doi.org/10.1006/adnd.1996.0006).
- [30] A. Adamczak, *Differential cross sections for muonic atom scattering from hydrogenic molecules*, Phys. Rev. A **74**, 042718 (2006), doi:[10.1103/PhysRevA.74.042718](https://doi.org/10.1103/PhysRevA.74.042718).
- [31] S. Agostinelli *et al.*, *Geant4—a simulation toolkit*, Nucl. Instr. and Meth. in Phys. Res. A **506**(3), 250 (2003), doi:[https://doi.org/10.1016/S0168-9002\(03\)01368-8](https://doi.org/10.1016/S0168-9002(03)01368-8).
- [32] T. J. Roberts and D. M. Kaplan, *G4beamline simulation program for matter-dominated beamlines*, IEEE Particle Accelerator Conference (PAC) pp. 3468–3470 (2007).
- [33] I. F. Silvera, *The solid molecular hydrogens in the condensed phase: Fundamentals and static properties*, Rev. Mod. Phys. **52**, 393 (1980), doi:[10.1103/RevModPhys.52.393](https://doi.org/10.1103/RevModPhys.52.393).
- [34] G. A. Fesenko and G. Ya. Korenman, *New results in the theory of muonic atom formation in molecular hydrogen*, Hyperfine Interact. **101/102**, 91 (1996), doi:[10.1007/BF02227609](https://doi.org/10.1007/BF02227609).
- [35] D. S. Covita *et al.*, *Line shape analysis of the  $K\beta$  transition in muonic hydrogen*, Eur. Phys. J. D **72**(4), 72 (2018), doi:[10.1140/epjd/e2018-80593-1](https://doi.org/10.1140/epjd/e2018-80593-1).
- [36] V. P. Popov and V. N. Pomerantsev, *Isotopic effects in scattering and kinetics of the atomic cascade of excited  $\mu^-p$  and  $\mu^-d$  atoms*, Phys. Rev. A **95**, 022506 (2017), doi:[10.1103/PhysRevA.95.022506](https://doi.org/10.1103/PhysRevA.95.022506).
- [37] V. P. Popov and V. N. Pomerantsev, *Collision-induced radiative quenching and other disintegration modes of the  $2s$  state of muonic hydrogen and deuterium atoms*, Phys. Rev. A **105**, 042804 (2022), doi:[10.1103/PhysRevA.105.042804](https://doi.org/10.1103/PhysRevA.105.042804).

- [38] M. Marszałek, *Multipass Cell for Laser Spectroscopy of Muonic Hydrogen*, Doctoral thesis, ETH Zurich, Zurich, doi:[10.3929/ethz-b-000587674](https://doi.org/10.3929/ethz-b-000587674) (2022).
- [39] M. Zeyen, *The Thin-Disk Laser System for the Measurement of the Ground-State Hyperfine Splitting in Muonic Hydrogen*, Doctoral thesis, ETH Zurich, Zurich, doi:[10.3929/ethz-b-000543614](https://doi.org/10.3929/ethz-b-000543614) (2021).
- [40] L. P. Sinkunaite, *Detection System for Measuring the Hyperfine Splitting in Muonic Hydrogen*, Doctoral thesis, ETH Zurich, Zurich, doi:[10.3929/ethz-b-000535935](https://doi.org/10.3929/ethz-b-000535935) (2022).
- [41] A. Adamczak *et al.*, *Muonic atom spectroscopy with microgram target material* (2022), [arxiv:2209.14365](https://arxiv.org/abs/2209.14365).